BIOCHEMISTRY
including biophysical chemistry & molecular biology

ARTICLE

pubs.acs.org/biochemistry

Steered Molecular Dynamics Simulations Reveal Important Mechanisms in Reversible Monoamine Oxidase B Inhibition

William J. Allen and David R. Bevan*

Department of Biochemistry, Virginia Tech, Blacksburg, Virginia 24061, United States

Supporting Information

ABSTRACT: The monotopic membrane protein monoamine oxidase B (MAO B) is an important drug target for Parkinson's disease. In order to design more specific, and thereby more effective, inhibitors for this enzyme, it is necessary to determine what factors govern inhibitor specificity and the inhibitor binding process, including the roles of the lipid bilayer, the active site loop, and several key residues within the binding pocket. Atomistic molecular dynamics simulations of MAO B either embedded in a lipid bilayer or free in solution have been performed. The simulations suggest that the bilayer controls the availability of the active site cavity by regulating the degree of fluctuation in two key loops that form the greater part of the active site entrance (residues 85−110 and 155−165). In turn, the enzyme itself causes local thinning and a decrease in area per lipid of the surrounding bilayer environment. Additional MD simulations of MAO B in complex with seven different reversible inhibitors followed by nonequilibrium steered MD simulations of the inhibitor unbinding have also been performed. The simulations demonstrate that the average energy of interaction between inhibitor and MAO B residues during inhibitor egress is an effective indicator of inhibitor strength and is also useful for identifying key residues that govern inhibitor specificity. These data provide researchers with valuable tools for designing effective MAO B inhibitors as well as outline a method that can be translated to the study of other enzyme−inhibitor complexes.

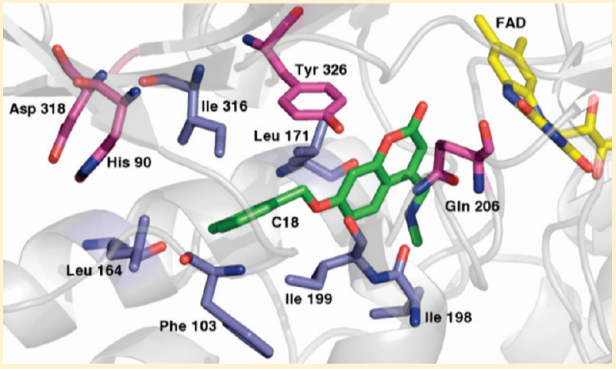

There are two isoforms of the enzyme monoamine oxidase (MAO): A and B. The latter (designated MAO B) regulates synaptic levels of certain amine neurotransmitters including phenylethylamine, benzylamine, and dopamine by oxidative deamination, a process that also results in the production of hydrogen peroxide.[1] MAO B expression increases with age, causing a decreased availability of dopamine and an increased degree of oxidative damage to neuronal cells by hydrogen peroxide—a pathway that, in combination with other factors, can lead to neurodegeneration and Parkinson's disease.[2] Treatment strategies have included supplementation with levodopa, a dopamine precursor, as a method to replenish depleted dopamine levels in patients showing parkinsonian-type symptoms. However, this treatment is only a temporary fix that does nothing to slow or reverse the progression of neuronal cell death.[3] For this reason, a wealth of research has been devoted to the development of effective MAO B inhibitors to be used as anti-neurodegenerative therapeutics.[3]

The irreversible MAO B inhibitors selegiline (L-deprenyl)[4] and rasagiline[5] are currently used as therapies to slow the progression, but not prevent Parkinson's disease. Additional studies have suggested that the effects elicited by selegiline and rasagiline are not solely due to MAO B inhibition, but instead a multitude of different pathways.[6] Newer reversible inhibitors, including safinamide and coumarin analogues, show some promise for their high specificity to the MAO B isoform.[7] As the general body of information grows, it is prudent to continue to design new MAO B inhibitors to be used as neuroprotectant therapeutics with higher specificities and fewer deleterious side effects. A detailed understanding of the specific molecular interactions that govern MAO B inhibition is essential to this process.

MAO B is a monotopic membrane protein embedded in the outer mitochondrial membrane. The 520-amino acid protein forms a homodimer with two helical tails that extend across the bilayer.[8] The bulk of the solvent-exposed part of the protein is divided into a region that covalently binds a flavin adenine dinucleotide (FAD) cofactor[9] and a region that houses the active site. The active site is dipartite, divided into a catalytic cavity that is proximal to the isoalloxazine ring of the FAD, and an entrance cavity that is positioned closer to the interface of the bilayer. Their combined volume is ~700 Å^3.[10] The crystal structure of MAO B was first solved in 2001 to 3 Å resolution.[8] There are now (as of March 2011) 36 unique crystal structures available in the Protein Data Bank[11] of MAO B and MAO B mutants in complex with different reversible and irreversible inhibitors, at as high as 1.6 Å resolution.[7]

Received: March 25, 2011
Revised: June 10, 2011
Published: June 20, 2011

Table 1. Summary of Inhibitor Structures Arranged by K_i

PDB code	res (Å)	inhibitor	abbrev	K_i (μM)	ΔG_{dissoc} (kJ/mol)[e]
1OJ9	2.3	1,4-diphenyl-2-butene	1PB	35[a]	26.4
2C67	1.7	*N*-methyl-1(*R*)-aminoindan	RM1	17[b]	28.3
1OJA	1.7	1*H*-indole-2,3-dione (isatin)	ISN	3[a]	32.8
2BK3	1.8	farnesol	FOH	2.3[c]	33.5
2V5Z	1.6	(*S*)-(+)-2-[4-(fluorobenzyloxybenzylamino) propionamide]	SAG	0.45 ± 0.13[d]	37.7
2V60	2.0	7-[(3-chlorobenzyl)oxy]-2-oxo-2*H*-chromene-4-carbaldehyde	C17	0.40 ± 0.02[d]	38.0
2V61	1.7	7-[(3-chlorobenzyl)oxy]-4-[(methylamino)methyl]-2*H*-chromen-2-one	C18	0.10 ± 0.02[d]	41.5

[a] Reference 18. [b] Reference 19. [c] Reference 13. [d] Reference 7. [e] Calculated by $\Delta G_{dissoc} = -RT \ln(K_i)$.

The wealth of available structural data makes this enzyme an ideal target for rational structure-based drug design.

Molecular dynamics (MD) is a useful computational tool that can offer insight into specific molecular interactions between protein and inhibitor at the atomic level—beyond what is learned from a static crystal structure. For example, crystal structures revealed that residues Ile 199[12,13] and Tyr 326[14] are important for ligand specificity. The "aromatic cage" formed by Tyr 398 and Tyr 435 plays a role in coordinating ligands in the active site to the FAD molecule.[15] In addition, the "active site loop" formed by residues 99−112 could be important in allowing ligand access to the active site.[8,16] Aside from these static-structure derived observations and predictions, one can uncover more about specific molecular processes and interactions using MD simulations. For example, Apostolov et al. recently demonstrated that the bilayer itself plays a role in influencing the dynamics of the MAO A isoform, especially with regards to the entrance to the active site.[17]

Here we have performed MD simulations of several different inhibitor−MAO B complexes in an attempt to better understand the nature and the mechanism of inhibition of this isoform. We sought to identify specific residues that contribute importantly to the binding of MAO B inhibitors, as well as identify behaviors, especially pertaining to the active site and active site entrance, which might also influence inhibitor binding. The resulting dynamic model of inhibitor binding and interaction within the active site is important in the design of novel anti-neurodegenerative therapeutics.

Scheme 1. Structures of MAO B Inhibitors Used in This Study

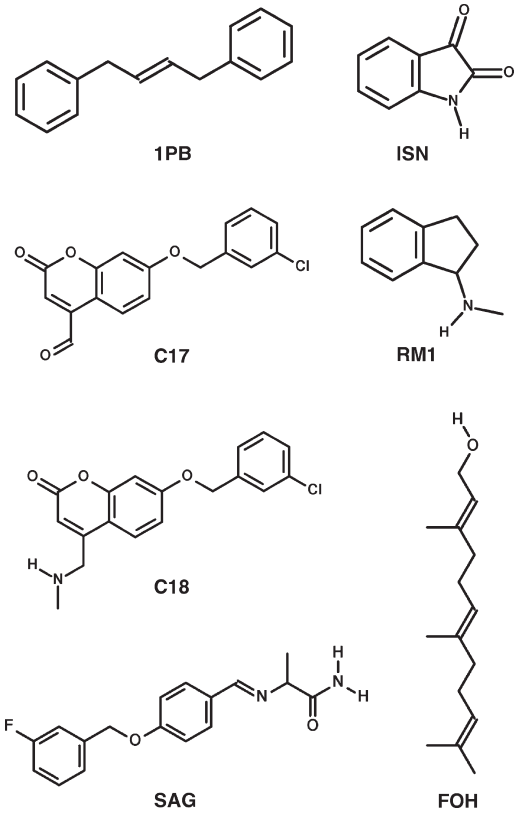

MATERIALS AND METHODS

File Preparation. Seven crystal structures were downloaded from the PDB: 1OJ9, 1OJA,[18] 2BK3,[13] 2C67,[19] 2V5Z, 2V60, and 2V61.[7] Each crystal structure consists of two protein chains (chains A and B) comprising the MAO B homodimer. Each chain is covalently bound to an FAD cofactor and contains a reversible inhibitor in the active site unique to the crystal structure. Important chemical information and inhibitor structures are summarized in Table 1 and Scheme 1. The K_i values were experimentally determined and originated from the corresponding citations in the footnote of Table 1; the ΔG_{dissoc} values were calculated as $\Delta G_{dissoc} = -RT \ln K_i$. In all cases, chain A includes residues Asn 3 to Ile 501 (Ile 501 is missing atoms), and chain B includes residues Asn 3 to Ile 496. The full-length homodimer contains 520 residues per chain; missing C-terminal residues were modeled in LEaP of the AmberTools 1.4 suite of programs,[20] and dihedral angles characteristic of an α-helix were imposed to correctly reflect the transmembrane nature of the residues. The two missing N-terminal residues were not modeled into the structure. Original crystal waters were removed from the PDB structures so that water molecules from the bulk solvent could diffuse into the active site during the forthcoming equilibration and production MD.

The protein topology was based on the united-atom GROMOS96 43A1 force field. The FAD topology was assembled from the existing adenosine triphosphate (ATP) and flavin mononucleotide (FMN) topologies in that force field. Inhibitor topologies were generated by the PRODRG server.[21] We previously showed that charges and charge groups generated by the PRODRG server are inconsistent with the GROMOS96 43A1 force field,[22] and accordingly the charges were refined either by analogy from existing groups in the GROMOS96 43A1 force field or by electrostatic potential calculations using the CHELP (*ch*arges derived from *e*lectrostatic *p*otential) model[23] at the Hartree−Fock level of theory with the 6-31G** basis set in Titan 1.0.8 (Wavefunction,

Inc., Irvine, CA). The FAD and small molecule topologies are included as Supporting Information (Tables S1−S8).

Lipid parameters[24] and the lipid bilayer starting structure[25] were obtained from the Biocomputing Group at the University of Calgary. The starting structure contained 128 pre-equilibrated palmitoyloleoylphosphatidylcholine (POPC) lipids arranged in a periodic cell. The system was multiplied into a 2 × 3 array along the $x-y$ plane, for a total of 768 lipid molecules, in order to create a sufficiently large foundation for the simulations. An in-house script was used to randomly select 329 lipids and then mutate the choline group to ethanolamine, thereby creating palmitoyloleoylphosphatidylethanolamine (POPE) molecules. The final lipid bilayer contained 439 POPC lipids and 329 POPE lipids, a 4:3 ratio that mimics the composition of the *in vivo* outer mitochondrial membrane[26] and a previous simulation.[16]

Conventional MD Simulations. All simulations were performed using GROMACS 4.0.7.[27] A twin-range cutoff was used to calculate short-range nonbonded interactions, with electrostatic interactions truncated at 0.8 nm and van der Waals interactions truncated at 1.4 nm. The particle mesh Ewald (PME) method[28,29] was used to evaluate long-range electrostatic interactions with fourth-order spline interpolation and a 0.12 nm Fourier grid spacing. All bond lengths were constrained using a parallelized linear constraint solver (P-LINCS),[30,31] and simulations were performed with a 2 fs time step. The simple point charge (SPC) water model was used.[32] Isochoric−isothermal (NVT) simulations employed the Berendsen thermostat[33] with a temperature coupling constant (τ_T) of 0.1 ps. Isothermal−isobaric (NPT) simulations employed the Nosé-Hoover thermostat[34,35] with a temperature coupling constant of 0.1 ps and a semi-isotropic Parrinello−Rahman barostat[36,37] with a temperature coupling constant (τ_P) of 1.0 ps and a compressibility of 4.5×10^{-5} bar^{-1} applied separately in the $x-y$ and z directions, a common practice for membrane simulations.[38]

The bilayer system was minimized with a steepest descents integrator until the maximum force on any atom was less than 1000 kJ mol^{-1} nm^{-1}. The system was then simulated under an NVT ensemble at 100 K for 200 ps. Following equilibration around the target temperature, the system was annealed to 310 K linearly over 900 ps under an NPT ensemble. Finally, a production simulation followed under the same conditions for 20 ns, with this final conformation of the bilayer simulations being used as the starting platform for protein insertion.

The seven crystal structures of MAO B described above were inserted into the bilayer using the "INFLATEGRO" methodology described by Kandt et al.[38] The apo-form of the crystal structure originating from PDB 1OJA (1.70 Å resolution) provided an eighth simulation condition that was simulated in triplicate. Minimization, equilibration, and production MD were performed in the same way as described for the bilayer. The protein backbone atoms were restrained until the production MD. These eight simulation conditions were then repeated in the absence of the bilayer, with the protein surrounded by bulk solvent (the apo-form was also simulated in triplicate). Following minimization, proteins simulated in a box of water were equilibrated at 310 K under an NVT ensemble for 200 ps, followed by 1 ns of NPT equilibration at the same temperature, and finally production MD as before. In the simulations of protein in bulk solvent, the pressure-coupling algorithm was applied isotropically, and weak restraints were imposed on the backbone atoms of the helical portion of the protein tail (residues 488−520). (Previous simulations in our lab demonstrated that performing MD with the transmembrane tails unrestrained in a box of solvent results in unnatural fluctuations between the protein subunits that consistently crashed the simulations; data not shown.) The tails were retained even in the absence of the lipid bilayer in case their proximity to the active site entrance was shown to be important.

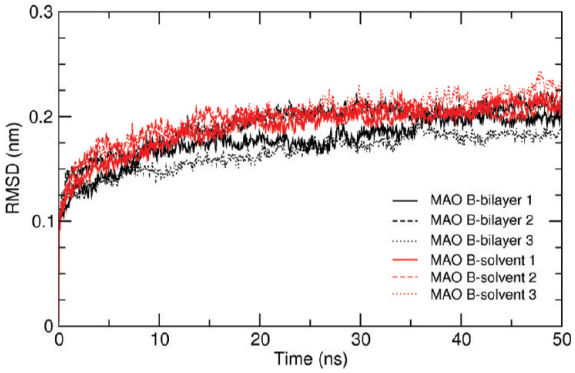

Figure 1. RMSD of the protein backbone, residues 1−485. The RMSD value is averaged over the two monomers in each replicate simulation.

Steered MD Simulations. Following production MD of inhibitor-bound systems, nonequilibrium pulling was performed independently on each reversible inhibitor in the direction of active site egress. In each case, the pulling simulation was performed in quintuplicate. The starting configurations and velocities for the pulling simulations were taken at 200 ps intervals. The direction of the unbinding vector was dynamically defined for each individual steered simulation based on the center-of-mass of the steered group and the center-of-mass of the active site entrance opening. The magnitude of the unbinding vector is automatically normalized in GROMACS. All constant-velocity steered MD simulations were implemented with a spring force constant of 1000 kJ mol^{-1} nm^{-2} and at a speed of 0.01 nm ps^{-1}.

Analyses were performed using utilities available in the GROMACS suite of programs or by scripts written in-house. Three-dimensional images were rendered with PyMol.[39] Chemical structures were created in PubChem Sketcher (http://pubchem.ncbi.nlm.nih.gov/), and two-dimensional line art was generated with Grace.[40] Bilayer thickness calculations and area per lipid (APL) were measured by the GridMAT-MD software[41] and plotted with Xmatrix (http://matpack.de/).

RESULTS

The simulation results will be discussed as follows. First, we discuss the triplicate, conventional MD simulations of MAO B in the apo-form. Thereafter, we will discuss the steered MD simulations of MAO B with inhibitors bound. Systems comprising MAO B in a bilayer will henceforth be referred to as MAO B-bilayer; systems of MAO B in bulk solvent will be referred to as MAO B-solvent.

Molecular Dynamics of MAO B. To obtain sufficient sampling, we simulated each replicate of MAO B-bilayer and MAO B-solvent under production MD conditions for 50 ns. When measured as a function of time, the root-mean-square deviation (RMSD) of a protein is a good indicator of the convergence in protein structure change over the course of a simulation. The MAO B transmembrane hydrophobic tails (residues 485−520) were restrained in the solvent simulations and therefore not considered for the RMSD calculations, nor were they considered for the RMSD calculations of the bilayer simulations for the sake

of consistency. The backbone RMSD of the MAO B-bilayer replicates equilibrated to between 0.19 and 0.21 nm after ~20 ns of simulation (Figure 1). Similarly, the backbone RMSD of each MAO B-solvent replicate equilibrated just slightly higher, between 0.21 and 0.24 nm, in the same time frame. The average RMSD over the last 30 ns of each set of three replicates was 0.19 ± 0.01 nm for MAO B-bilayer and 0.22 ± 0.01 nm for MAO B-solvent. The relative stability of each structure after the first 20 ns provides assurance that the final 30 ns of simulation are suitable for analysis. It is useful to note that the backbone RMSD of the full-length bilayer-bound MAO B (data not shown) was not appreciably different from that of the RMSD measured without considering the hydrophobic tails (Figure 1), confirming our decision to perform analyses on the final 30 ns of simulation.

As RMSD is a global measurement of protein motion, root-mean-square fluctuation (RMSF) is a local measurement that provides a higher resolution detail of residue fluctuations. Each of the triplicate simulations contained the full homodimeric form of MAO B, thus providing six individual monomers for analysis. During the last 30 ns of simulation, the differences in fluctuation pattern between MAO B-bilayer and MAO B-solvent in two particular regions of the enzyme demanded further investigation. These regions were residues 85−110, which includes most of the active site loop (residues 99−112), and residues 155−165. A representative RMSF plot is shown in Figure 2a (the other RMSF plots are included as Supporting Information in Figure S1). On average, the degree of fluctuation exhibited by these two regions was larger for MAO B-solvent than it was for MAO B-bilayer. The fluctuation from residues 85−110 was 0.10 ± 0.03 nm when in a bilayer and 0.16 ± 0.06 nm when in solvent, a statistically significant increase as determined by a Student's *t* test ($p < 0.05$). The fluctuation from residues 155−165 was 0.081 ± 0.019 nm when in a bilayer and 0.101 ± 0.036 nm when in solvent, also statistically significant by the same test ($p < 0.05$). No other areas in the protein were consistently higher or lower in fluctuation. This observation is particularly significant because these two regions form the entrance to the active site cavity (Figure 2b), indicating that the bilayer exerts a degree of control over the fluctuations of these loops and subsequently the interactions that may occur in these regions.

As these two loop regions comprise the ringlike "mouth" of the active site, it is convenient to then define the size of the active site entrance by measuring the best-fit ellipsoidal surface area formed by opposing residues in the loops. Thus, the center-of-mass distance between Lys 93 and Trp 107 was treated as one axis of the ellipse, and the center-of-mass distance between Tyr 97 and Ser 160 was treated as the second axis. This concept is illustrated in Figure 3. It stands to reason that a larger ellipsoidal surface area would be reflective of a more open conformation, while a smaller surface area would indicate a more closed conformation. The following equation was used to calculate the surface area of the active site entrance opening:

$$\text{surface area} = \pi\left[\frac{1}{2}(\text{Lys } 93 - \text{Trp } 107)\right]\left[\frac{1}{2}(\text{Tyr } 97 - \text{Ser } 160)\right]$$

The residue names in the equation refer to the center-of-mass position of those residues. The resulting surface area of each active site entrance is plotted with respect to time in Figure 4. In the MAO B-bilayer simulations, five of the six replicates converged to an active site entrance opening between 1.00 and 1.50 nm. One

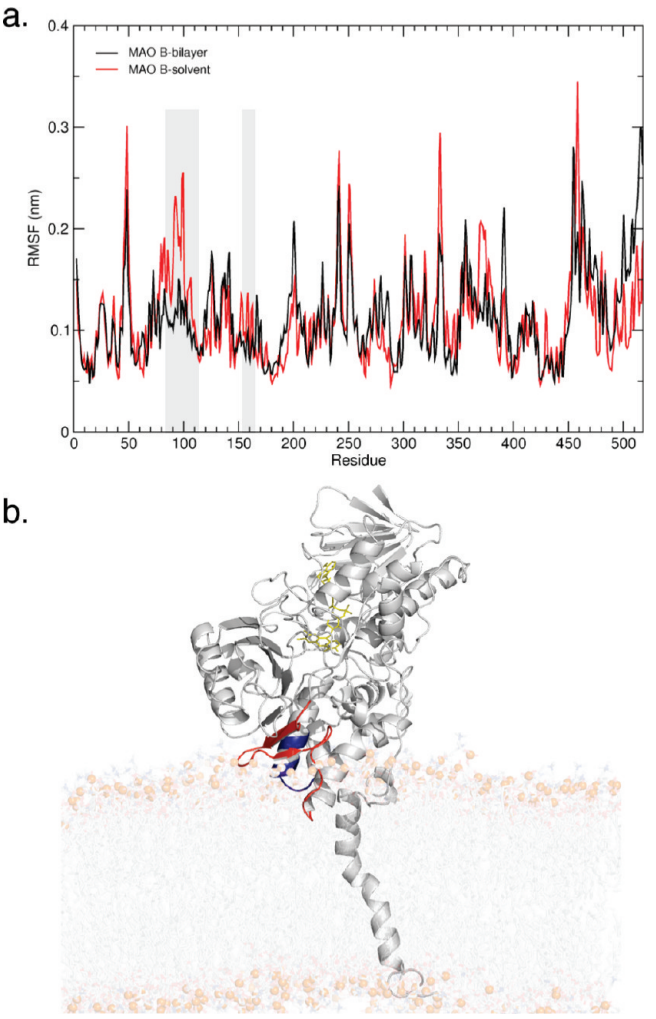

Figure 2. A representative RMSF plot is shown in panel (a). Two regions of the protein backbone exhibit fluctuations that are dependent on the local environment (embedded in a bilayer or exposed to solvent), residues 85−110 and 155−165. These regions are highlighted with gray bars. An example snapshot of MAO B embedded in a bilayer is shown in (b). The regions of protein that fluctuate differently depending on the local environment are colored differently; residues 85−110 are highlighted red, and residues 155−165 are highlighted blue. The bilayer was made transparent, and the phosphorus atoms are represented as orange spheres. The FAD cofactor is shown as yellow sticks. One MAO B subunit and water atoms were removed for simplicity.

replicate of MAO B-bilayer, however, demonstrated a behavior that could be described as the opening of the active site entrance. The size of the opening in replicate 1, chain B, increased to more than 2.25 nm^2, in the presence of the bilayer. We found that MAO B-solvent typically maintained an active site entrance surface area between ~0.75 and 1.50 nm^2 during the simulations. Further, the fluctuation in this value was greater than it was for MAO B-bilayer, reflecting the previous observation that MAO B in the absence of the bilayer exhibited a higher RMSF in these regions. These data provide further evidence that the lipid bilayer regulates behaviors that occur near the entrance to the active site.

To further explore how the lipid bilayer modulates the fluctuation of these loops and to understand the mechanism by which the active site mouth opens and closes, we examined more closely the interaction between the protein and the bilayer. Qualitative

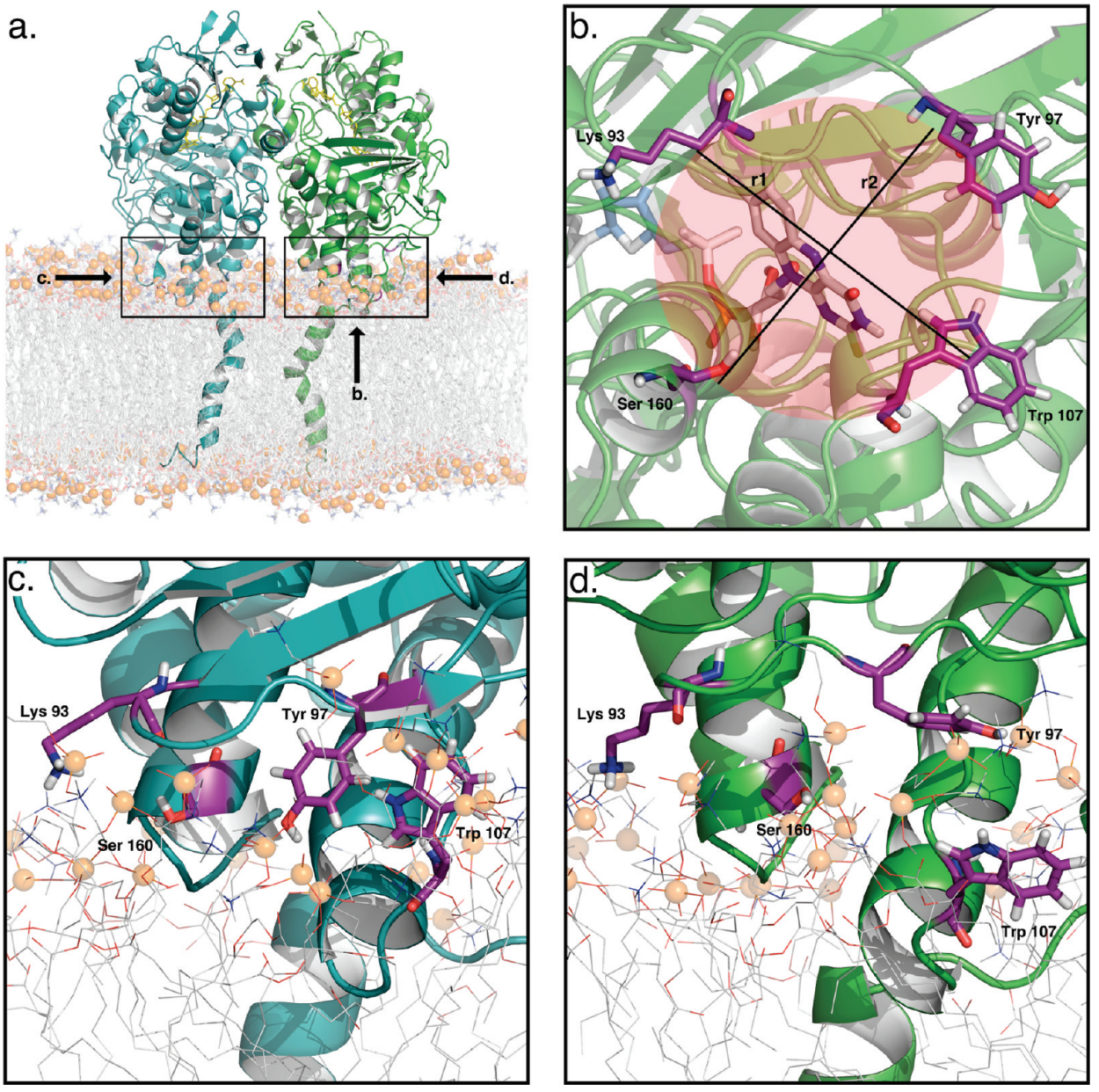

Figure 3. (a) Overview of MAO B homodimer embedded in a lipid bilayer. Each arrow indicates the direction from which the subsequent panels are viewed. (b) A view into the active site with opposing residues shown. Ellipse approximates active site entrance opening area. (c, d) Active site opening residues shown in a closed (c) and open (d) conformation.

analysis of the MD simulations indicated that the protein active site entrance that opened in the presence of the bilayer did so because it dipped down below the lipid head groups toward the hydrophobic fatty acid tails. In doing so, native interactions between residues in the loops were disrupted and new interactions with the hydrophobic tails were formed. Figure 3 compares two active site entrances: that of a closed conformation (Figure 3c) and that of an open conformation (Figure 3d). From the snapshot of the open conformation we can see that the Tyr 97 moved up away from the bilayer so the plane of the aromatic ring was parallel to the surface of the bilayer and the Trp 107 moved further down into the bilayer, forming hydrophobic contacts with the lipid tail. In the closed conformation, these two residues formed π-stacking interactions with one another. In addition, the Lys 93 and Ser 160 residues snorkeled into the lipid headgroups in the closed conformation, whereas the same residues were further into the aqueous phase in the open conformation.

A measurement of partial densities as a function of the bilayer normal established a quantifiable and time-averaged comparison between closed and open conformations. The partial densities of each lipid component, the bulk of the protein, and the active site entrance of each monomeric subunit were measured (Figure 5). The key observation lies in the positioning and shape of the active site entrance in the open conformation. Its position was shifted along the *z*-axis, further into the bilayer, creating a bimodal peak. Because the active site entrance of the other subunit within the dimer remained closed, one possible explanation is that the enzyme tilted with respect to the plane of the bilayer. Also, because all of the active site entrances in the MAO B-solvent replicate simulations remained in the closed conformation, we

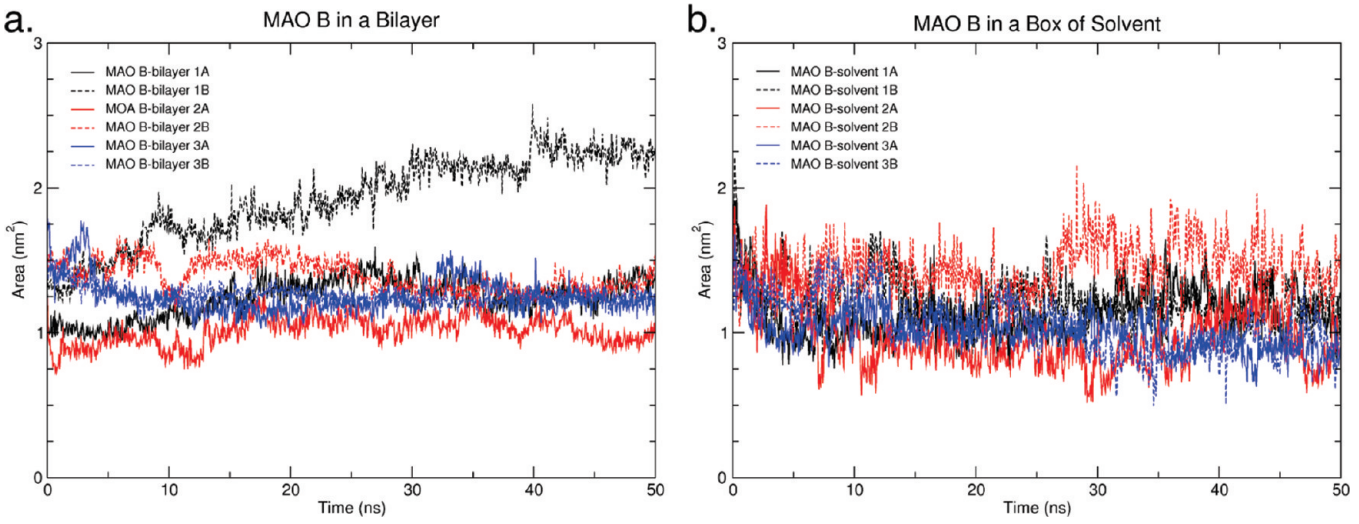

Figure 4. Comparison of the area of the active site channel opening when MAO B is in a bilayer (a) vs MAO B in a box of solvent (b).

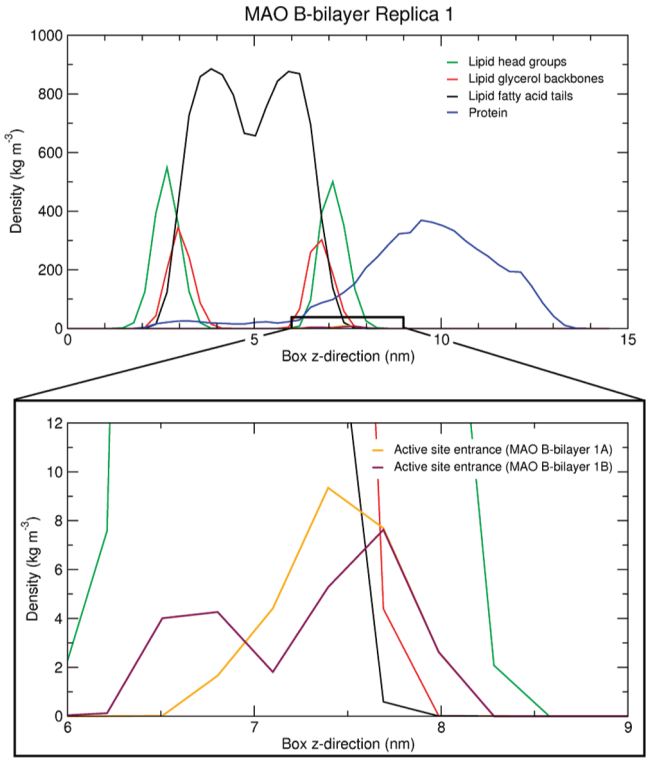

Figure 5. Partial density plot for important lipid and protein components along the *z*-axis. Inset is a close-up of the active site entrance opening residues. The residues considered for this measurement are Lys 93, Tyr 97, Trp 107, and Ser 160.

can hypothesize that it is the formation of new hydrophobic interactions that facilitated the active site entrance-opening event. Table 2 shows the average height of the center-of-mass of the active site entrance opening with respect to the average position of the phospholipid headgroups. In each replicate, the average position of one of the active site mouths of the dimer dipped down with respect to the phospholipid heads, from 0.12 to 0.16 nm. The other chain in the same replicate stayed above the phospholipid headgroup, near 0.32−0.33 nm. In a single replicate, the active site entrance residues that dropped below the headgroups shifted into the open configuration, suggesting that interactions within this hydrophobic region control the size of the active site entrance. We note that the distance of the active site mouth to the bilayer surface did not always result in an observable opening of the active site (Figure 4a). This is likely due to the short time frame of our simulations relative to the apparently slow period of active site channel opening and closing, and thus it would be improbable to observe this behavior in all replicates without applying nonphysiological techniques such as locally enhanced sampling or greatly extending the length of the simulations.

An alternative method to quickly increase the probability of active site entrance opening is to mutate residues responsible for keeping the active site entrance in the closed conformation. We hypothesized that by mutating Tyr 97 to glycine, loss of the π-interaction between Tyr 97 and Trp 107 would result in Trp 107 extending into the hydrophobic portion of the bilayer more readily. We simulated a Y97G mutant form of MAO B in a bilayer in triplicate as described in the Materials and Methods. As a result, we observed the active site entrance opening event in only one monomer in each of the three replicate simulations. In all simulations, the active site entrance of the monomer that was tilted lower with respect to the plane of the bilayer moved into the open conformation in part because Trp 107 extended into the hydrophobic part of the bilayer (Figure S2). In the mutant systems, the opening process occurred very rapidly during the 1.2 ns of equilibration prior to production MD. This observation supports our hypothesis that the active site entrance opening event itself is reproducible and occurs in accordance with enzyme tilting.

In addition to the effects elicited by the bilayer on the active site entrance, the enzyme itself also changed the local structure and dynamics of the bilayer such that it may be more conducive to inhibitor or substrate trafficking. Foremost, over the last 30 ns of simulation, the average bilayer thickness was notably decreased around MAO B when compared to a control bilayer (Figure 6). The control bilayer ranged in thickness (phosphorus atom−phosphorus atom) from 3.93 to 4.55 nm (excluding outliers), and the average bilayer thickness was 4.3 ± 0.2 nm, a value that is slightly thicker, but still in good agreement with previously reported X-ray scattering data of 3.70 nm for POPC[42] and 4.13 nm for pure POPE.[43] In the presence of MAO B, however, the bilayer

Table 2. Position of Important Groups along *z*-Coordinate

replica	lipid head (nm)	glycerol (nm)	entrance to active site A (nm)	entrance to active site B (nm)
1	0	−0.35	+0.33	+0.16
2	0	−0.25	+0.33	+0.12
3	0	−0.35	+0.13	+0.32

thickness increased in range to 3.64−4.75 nm (excluding outliers). Although the average remained the same, the standard deviation increased (4.3 ± 0.3 nm), which results from the larger extremes of thickening or thinning. This observation is best illustrated by the fact that there were two large pockets in close proximity to MAO B that exhibited a large amount of thinning. This observation is consistent for 5 of the 6 monomeric subunits. One monomer in the third replicate seemed to have no major effect on the thickness of the bilayer that immediately surrounds it, suggesting that the degree of thinning may not always be evident. Coinciding with bilayer thinning, we also observed kinking of the MAO B transmembrane α-helices. Kinking itself is very common among transmembrane helices and is likely due to hydrophobic mismatch.[44] In any case, the tail conformations still spanned the membrane, as would be expected.[45]

The presence of MAO B also influenced the area per lipid headgroup (APL) of the bilayer systems. The control bilayer maintained an average APL of 53.8 ± 0.2 Å^2 per leaflet during simulation. Once MAO B was inserted, the average APL in the top leaflet dropped to 50.2 ± 0.6 Å^2 ($p < 0.05$) and the average APL in the bottom leaflet dropped to 51.7 ± 0.5 Å^2 ($p < 0.05$), as averaged over the last 30 ns of simulation. The previously reported experimental APL for pure POPC is 68.3 Å^2 [42] and 56 Å^2 for pure POPE.[43] The APL of the control bilayer converged slightly below these numbers because the ethanolamine and choline headgroups have a cooperative fit when mixed together. The closer packing also forces the tails to be slightly more ordered, accounting for the increased APL observed.

Steered Molecular Dynamics of MAO B Inhibitors. In addition to the simulations of apo-MAO B embedded in a bilayer and in bulk solvent, we performed several simulations of MAO B in complex with various reversible inhibitors. Herein, the inhibitors will be referred to by a three-letter identifier, which they were assigned in the PDB (summarized in Table 1 and Scheme 1). Following a preliminary 20 ns production run of these inhibitor-bound systems, we saved full atomic coordinates and velocities in 200 ps increments. These snapshots served as starting points for nonequilibrium steered MD simulations, as described in the Materials and Methods. In this study we employed constant velocity pulling. Briefly, the inhibitor was tethered to a dummy atom (an atom having neither mass nor charge) by a classical spring. The dummy atom traveled along a prespecified vector at a constant velocity. As tension in the spring increased, the inhibitor was steered away from its original position, along the same general path as the vector. The force in the spring was recorded with respect to time or displacement of the inhibitor. We performed five such steered simulations for each inhibitor in each condition (bilayer and solvent), for a total of 70 simulations.

During a steered simulation, the force required to pull each inhibitor was plotted as a function of displacement from the original position, or distance traveled from the binding site, for each simulation (Figure 7). By integrating each curve, we obtained the work performed on the system for each simulation.

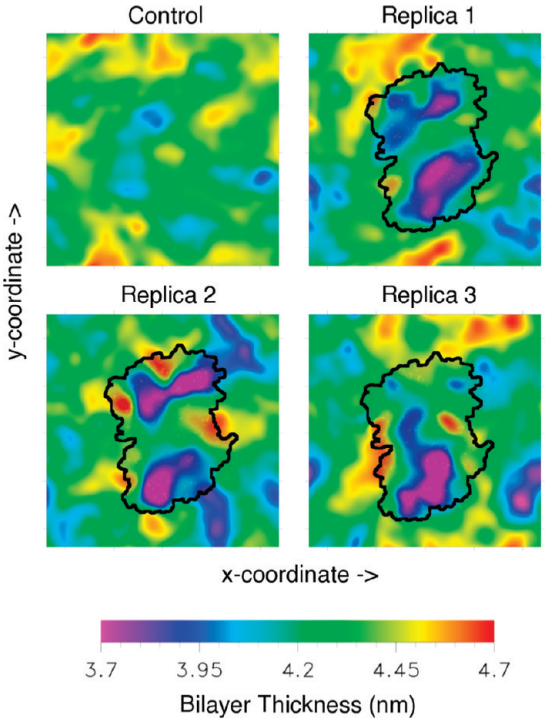

Figure 6. Bilayer thickness plots. The top left plot is a top-down perspective thickness plot of a control bilayer. The remaining three plots are the thicknesses of the replicate simulations. The position of the MAO B homodimer is overlaid as a black, transparent surface.

Jarzynski's equality[46] equates the average work performed on replicate ensembles to the potential of mean force (ΔPMF) for a nonequilibrium process or the overall change in free energy between two states along a reaction coordinate:

$$exp(-\Delta PMF/k_B T) = \langle exp(-W/k_B T)\rangle$$

In Jarzynski's equality, W is the work performed on a system, k_B is the Boltzmann constant, and T is temperature in kelvin. The angled brackets signify an average over ensembles. We considered the beginning of the reaction coordinate to be the MAO B-inhibitor complex and the end of the reaction coordinate to be the state in which the distance of separation from any inhibitor atom and any protein atom was greater than or equal to 0.7 nm.

From these data it is convenient to make two important comparisons: the pulling of different inhibitors into the same media (bilayer, for example) and the pulling of the same inhibitor into two different media (bilayer and solvent) (Figure 7 and Table S9). For example, pulling the weak inhibitor 1PB into the bilayer required a peak force of 606 ± 36 kJ mol^{-1} nm^{-1}, whereas pulling the strong inhibitor C17 into the same media required a greater peak force, 730 ± 82 kJ mol^{-1} nm^{-1}, a statistically significant increase ($p < 0.05$). Conversely, the inhibitor 1PB required a peak force of 373 ± 35 kJ mol^{-1} nm^{-1} to pull into solvent, a much smaller amount than was required to pull the same inhibitor into the bilayer. In fact, all seven of the inhibitors required a smaller peak force to pull into solvent with the exception of ISN. It is convenient to plot the Gibbs free energy of dissociation (ΔG_{dissoc}) of each inhibitor by the greatest (peak) force required to pull the inhibitor from the binding site (Figure S3). The best-fit linear regression of that plot had a positive slope in each case, that is, the greatest amount of force required to pull an inhibitor from the

dx.doi.org/10.1021/bi200446w |*Biochemistry* 2011, 50, 6441–6454

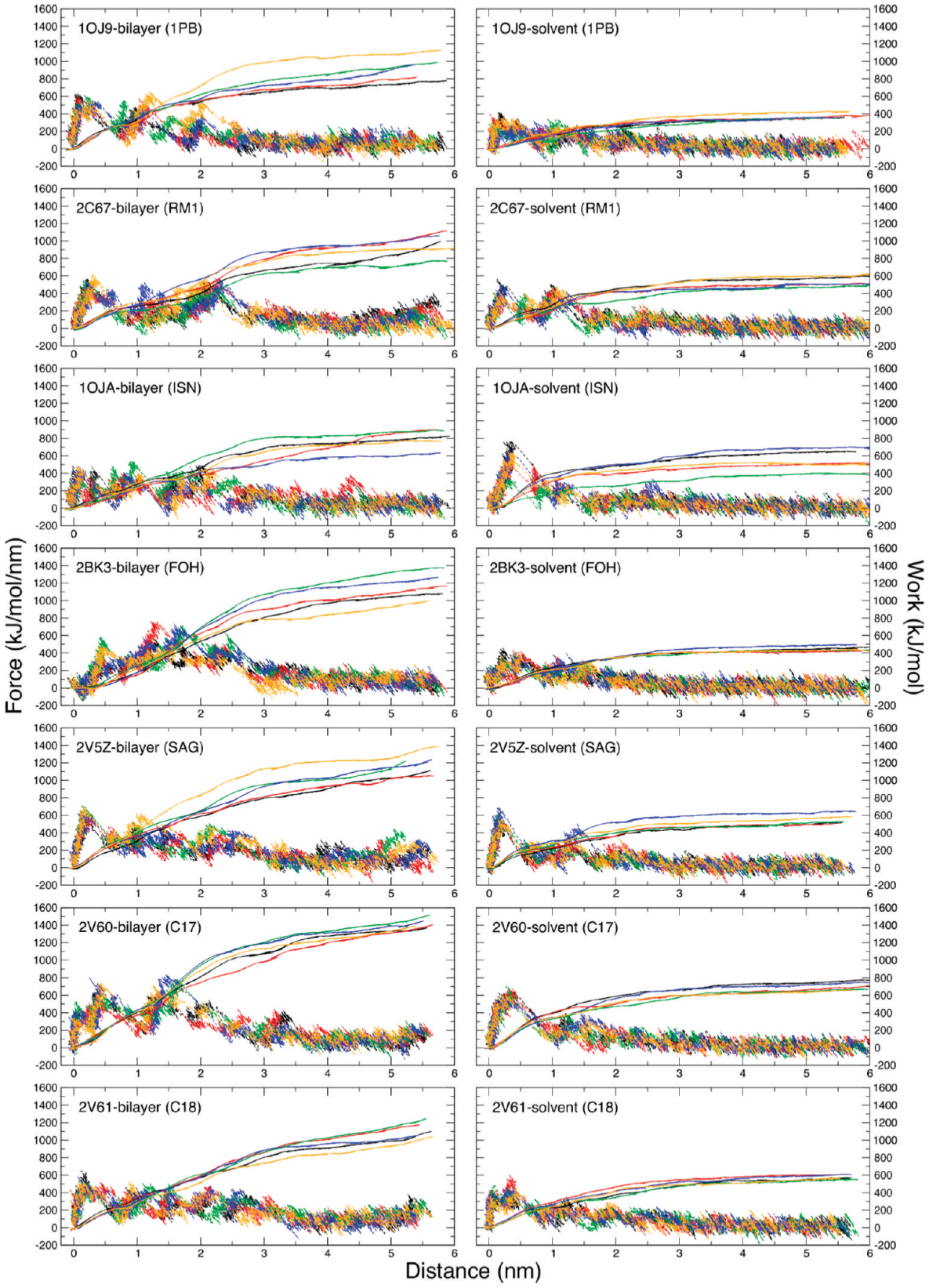

Figure 7. ΔPMF plots for inhibitor unbinding. The plots in the left column are bilayer simulations, and the right column are solvent. The five replicates are colored differently (black = 1, red = 2, green = 3, blue = 4, orange = 5). The smooth, summative curves are integrals of the irregular curves, corresponding to work, displayed on the right axis.

binding site increased with increasing strength of the inhibitor. However, the correlation coefficient values were quite low: 0.04 for pulling into the bilayer and 0.27 for pulling into solvent. Although there is no strong correlation between the strength of

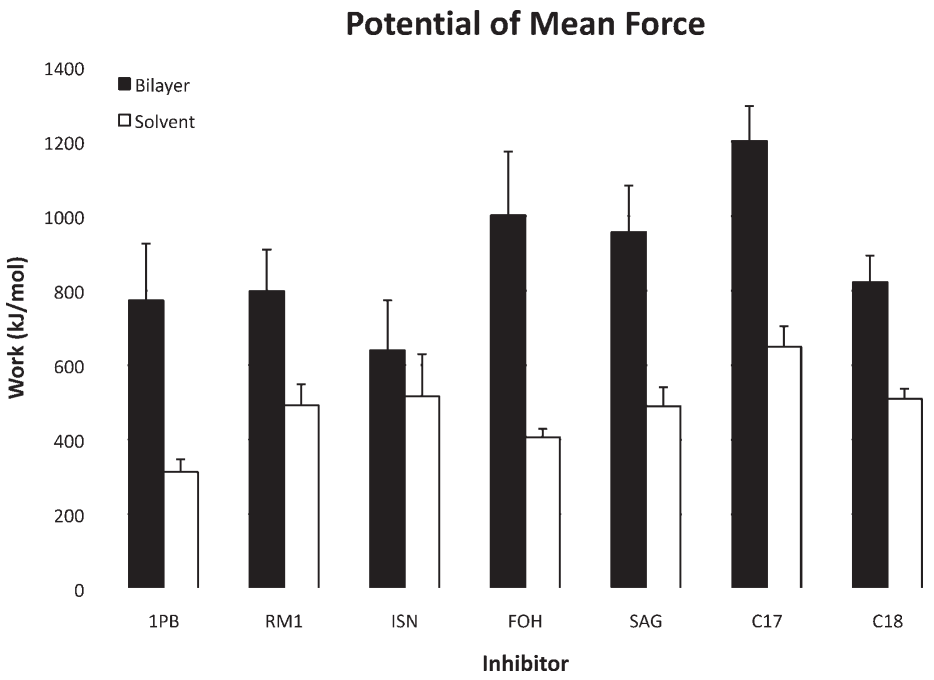

Figure 8. Average ΔPMF values for pulling inhibitors from the protein active site. Black bars represent inhibitor being pulled into the bilayer, and white bars represent inhibitor being pulled into solvent. Inhibitors are arranged from left to right by increasing magnitude of ΔG_{dissoc}.

each inhibitor and the peak force required to pull, the general increase in force required between solvent and bilayer is apparent. At first glance it seems as if pulling into different media itself would cause the discrepancy; however, we find that the peak force typically occurs while the inhibitor is still deep within the binding pocket, before it encounters solvent or bilayer. Therefore, it stands to reason that the medium itself may allosterically regulate the dynamics of residues in the binding pocket.

The ΔPMF of pulling 1PB, the weakest inhibitor, into the membrane was 770 ± 150 kJ mol^{-1}, as averaged over five simulations (Figure 7 and Table S9). Conversely, the ΔPMF of pulling C17, a very strong inhibitor, into the membrane was 1201 ± 94 kJ mol^{-1}, a statistically significant increase ($p < 0.05$). The two ΔPMF values of the weak inhibitors RM1 and of ISN fell below 800 kJ mol^{-1}. The ΔPMF of ISN was particularly low, which could be attributed to its diminutive size compared to the other inhibitors. The two ΔPMF values of two of the strongest inhibitors, FOH and SAG, were above 1000 and 950 kJ mol^{-1}, respectively. The inhibitor C18 seemed to be the most bothersome outlier, with a ΔPMF of 823 ± 72 kJ mol^{-1}. It is difficult to determine the exact reason for the discrepancy, but it must be attributed to interactions between the secondary amide group and surrounding residues, for this group is the only difference between C18 and the structure of C17. In Figure 8, the average ΔPMF values required to pull each inhibitor into solvent or bilayer are arranged by the strength of the inhibitor. The correlation between ΔG_{dissoc} and ΔPMF is slightly higher than it is for ΔG_{dissoc} and peak force and thus is a slightly better rubric for measuring the validity of the simulations. The best-fit linear regression for pulling inhibitors of different strength out of the binding pocket and into the bilayer or solvent are both positively sloped and have correlation coefficients of 0.19 and 0.40, respectively (Figure S4). Although the correlation is still quite low, the increase in correlation does indicate that the total amount of work performed on a system is a better indication of inhibitor strength than is the peak amount of force applied. In addition to the slightly improved correlations, we also observed a greater separation of data between pulling into the bilayer or solvent. For every inhibitor, it required more work to pull into the bilayer than it did to pull into solvent. The ΔPMF of pulling each inhibitor into bulk solvent is drastically decreased when compared to pulling each inhibitor into the bilayer. There are two simple explanations for why such a difference could occur: a decrease in force required to pull through the media (bilayer vs solvent) or a decrease in interaction between the protein and inhibitor because the change in environment has made the protein less conducive to inhibitor binding. To address the first explanation, when the inhibitor was pulled through just media (between roughly 350 and 550 ps in Figure 7), the force required to pull through the bilayer was only 40−70 kJ mol^{-1} nm^{-1} higher on average. It is unlikely that simply the entrance into the media resulted in a change in work as great as observed for some inhibitors (Figure 8). In fact, to account for a 400 kJ mol^{-1} change in work, one would need to pull through the more viscous media an extra distance of 6−10 nm, much further than they were pulled in the actual simulation. Thus, it is likely that the change in medium from bilayer-bound to solvent-exposed effectively decouples native protein−ligand interactions that are typically occurring. These observations attest to the importance of studying the inhibitor−protein complex in the most appropriate physiological environment.

Quantification of average energy of interaction between each inhibitor and specific residues in the MAO B active site channel provided an excellent indication of which residues were important in inhibitor binding. For each steered MD simulation, we tabulated all MAO B residues that were within 0.7 nm of the inhibitor at any time. Then, the van der Waals and electrostatic contributions to the potential of interaction between inhibitor and individual residues were recorded. Finally, for each residue we took an average of any value that was above a 0.01 kJ mol^{-1} cutoff and plotted those interactions that contributed the most to the protein−inhibitor interaction (Figure 9). Some inhibitors

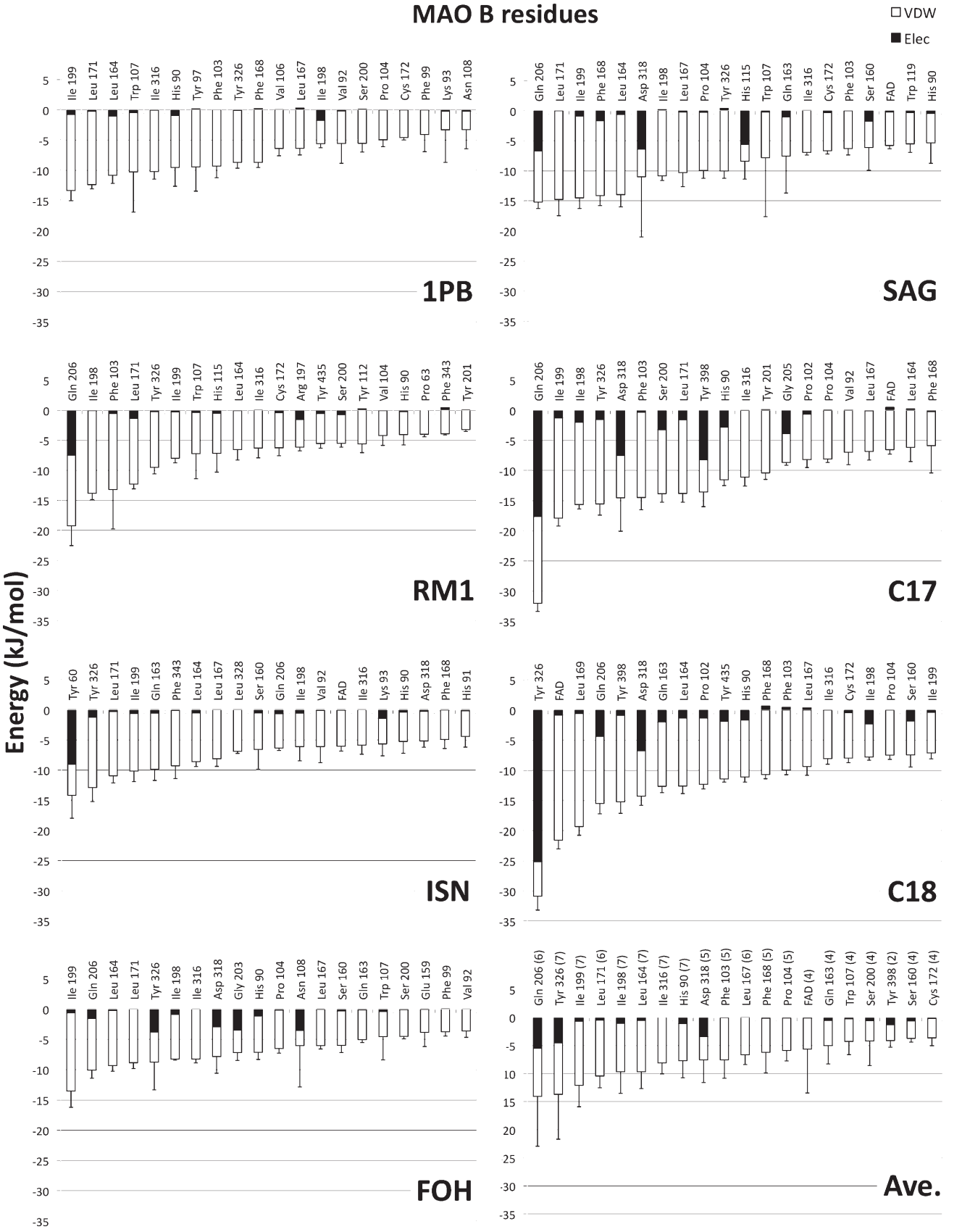

Figure 9. Summated and averaged energies of interaction between specific inhibitors and MAO B when pulling in a bilayer. The black component of each bar represents electrostatic interactions, and the white component represents van der Waals interactions. The final panel is an average of the other seven panels.

dx.doi.org/10.1021/bi200446w |*Biochemistry* 2011, 50, 6441–6454

interacted with as many as 45 different MAO B residues during active site egress, but we plotted only the 20 strongest interactions for simplicity. The weakest inhibitor, 1PB, had a total interaction of -176 ± 12 kJ mol^{-1} with MAO B residues. The total energy of interaction increased in magnitude for each sequentially stronger inhibitor, with the exception of the inhibitor FOH at -277 ± 10 kJ mol^{-1} and the inhibitor C18 at -270 ± 6 kJ mol^{-1}. In Figure 10, we arranged the sums of the individual energy components by increasing strength of the inhibitor. Most encouragingly, the sums of the individual energy components correlated strongly with the ΔG_{dissoc} of the inhibitor (Figure S5). The correlation coefficient for the best-fit linear regression that describes the increasing potential of interaction (increasing in magnitude, that is) with increasing inhibitor strength is 0.67. Notably, the correlation coefficient for the same relationship, but only considering the electrostatic contributions, is 0.86. The implication here is that the addition of electrostatic interactions contributes most meaningfully to the increased strength of the inhibitor.

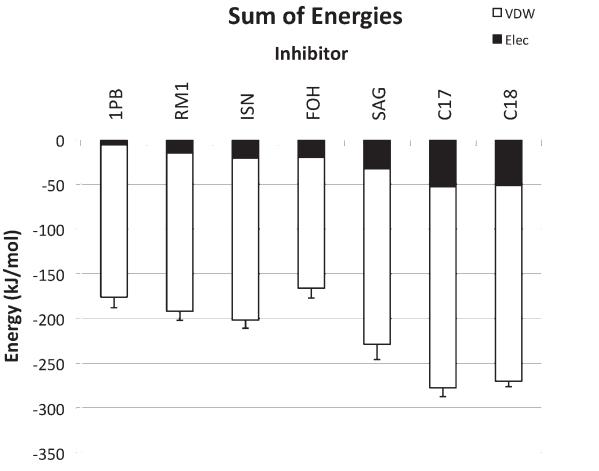

Figure 10. Sum of binding energy components for each inhibitor. The black part of each bar corresponds to electrostatic interactions, and the white part of each bar corresponds to van der Waals interactions. Inhibitors are arranged from left to right by increasing magnitude of ΔG_{dissoc}.

From analysis of the energies of interaction, we are also able to identify residues and specific interactions that may be important to inhibitor binding. The last panel in Figure 9 summarizes the average energy of interaction between MAO B residues and all inhibitors. The number in parentheses following the inhibitor name in the final panel of Figure 9 indicates the frequency with which that residue appeared in the other top-20 plots. The three strongest-interacting residues are Gln 206, Tyr 326, and Ile 199 (Figure 11). It is evident that a strong electrostatic contact near the site of Gln 206 or Tyr 326 (both of which sit above the active site very near to the FAD cofactor) is a core component that helps account for a large ΔG_{dissoc} value. Further, a strong and large contribution to the interactions in the hydrophobic core is also essential to good inhibition. Of the top ten contributing residues, six are hydrophobic, five of which line the bottom of the active site and active site channel. Finally, His 90 and Asp 318 are also two important polar residues that contribute to the binding of the inhibitor. All of the inhibitors examined in this study bind adjacent to the FAD molecule in the back of the active site. From this position, these inhibitors are too short to form contacts with His 90 or Asp 318, which are positioned closer to the active site entrance. This indicates that the inhibitors only started interacting

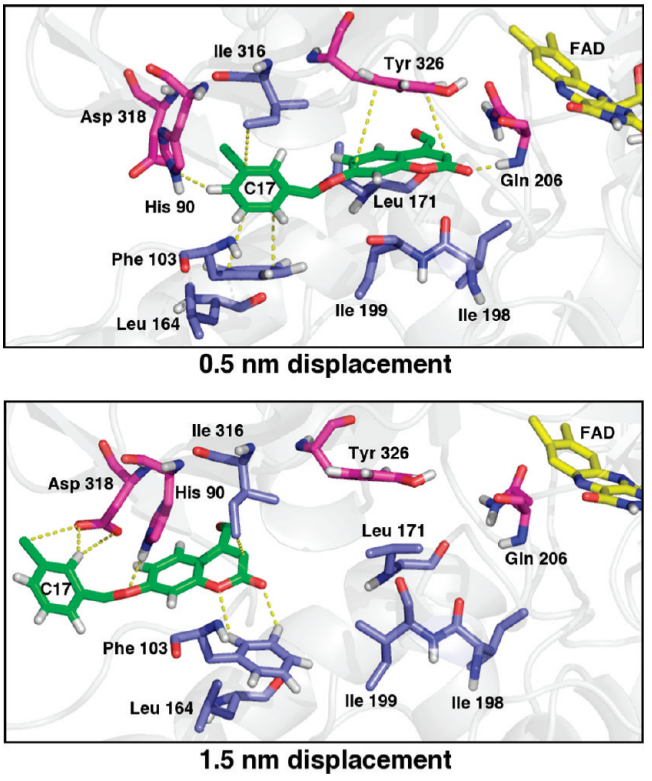

Figure 11. View of the MAO B active site during inhibitor C17 (green) egress at 0.5 nm displacement (top) and 1.5 nm displacement (bottom). Contacts between the inhibitor and hydrophobic (blue) or polar (red) residues under 4 nm are shown as yellow dashes.

dx.doi.org/10.1021/bi200446w |*Biochemistry* 2011, 50, 6441–6454

with these residues during the active site egress. Therefore, it would make sense to design an inhibitor that is larger and contains the appropriate group to form electrostatic contacts or hydrogen bonds with His 90 and Asp 318. Finally, we must remember that although several of the electrostatic contacts are tempting to exploit, most of the restoring force comes from hydrophobic van der Waals type contacts, which should be the focus of any pursuit in inhibitor design.

To better characterize those specific interactions that are important to inhibitor binding and to validate the model for inhibitor design proposed above, we briefly return to Figure 7. The peaks in the force curves correspond to different bound states of the inhibitors; the greater the height of the peak, the more tightly it is bound. Therefore, it is useful to examine what specific interactions were occurring at the tallest peaks and what interactions broke causing the downward slope in the curves. Presumably, at the top of the force peaks, the inhibitors should be most closely interacting with those residues identified as important in Figure 9. In fact, that is the case. For example, we examined the egress of C17 from the MAO B-bilayer active site. There are two notable peaks that occur during inhibitor egress: one at ~0.5 nm displacement and another at 1.5 nm displacement (Figure 7). At 0.5 nm displacement, C17 formed hydrogen bonds with Gln 206 and His 90, π-stacking interactions with Phe 103 and Tyr 326, and van der Waals interactions with Leu 171, Ile 198, Ile 199, and Ile 316. Therefore, the height of that first peak is a measure of the force required to overcome these interactions. Immediately past the tip of the first peak, those interactions were broken and the ligand moved further through the active site. At 1.5 nm displacement, the ligand formed electrostatic contacts with Phe 103, His 90, and Asp 318 and van der Waals contacts with Ile 316. The break in this second peak corresponded to a disruption in these specific interactions and total egress from the active site (Figure 11). This trend holds true for the other six inhibitors. In general, and especially in the case of the inhibitors with lower K_i values, the residues that are responsible for binding the inhibitor the most tightly are those that were identified as important by the energy profile in Figure 9. Increasing the strength of future inhibitors now becomes an exercise in modifying specific functional groups to optimize the strength of these interactions.

DISCUSSION

We performed classical MD simulations of the MAO B homodimer in a POPC−POPE mixed bilayer and in bulk solvent, followed by steered MD simulations of several reversible MAO B inhibitors also in bilayer or solvent. Taken together, these data effectively describe the mechanism of inhibition of MAO B by reversible inhibitors and the role of the bilayer in governing the dynamics of MAO B—especially around the active site entrance.

The dynamics of two specific loops, residues 85−110 and 155−165, are closely modulated by the bilayer. Previously, it was suggested that the "active site loop", residues 99−112, is important in inhibitor specificity.[8] From our observations, it seems the modulation of the loop by the bilayer is a control mechanism in which the protein and bilayer work in a concerted effort to control ligand binding. The bilayer modulates these two loops by facilitating the transition between an open and a closed conformation. Fowler et al.[16] suggested that perhaps MAO B undergoes a periodic tilting. While we did not find conclusive evidence to support or refute this hypothesis, we believe it could explain some behaviors we observed. When one active site entrance dipped down into the hydrophobic core of the bilayer, the change in the nature of the environment disrupted key interactions between residues at the mouth of the active site, facilitating the transition into the open conformation. We observed a dipping motion in these key active site residues with respect to the bilayer, and we found that the protein tended to be tilted with respect to the height of the active site entrance along the *z*-dimension. Previously, Apostolov et al.[17] examined a similar model, the monomeric MAO A isoform, and observed that the bilayer modulates the dynamics of the protein and, subsequently, ligand binding. However, they found that the same active site loop region (residues 105−115) fluctuates *more* in a bilayer, not less as we observed for MAO B. This difference could be due to subtle differences in the sequence between the MAO A and B isoforms and may contribute to their distinguishing ligand specificities. The bilayer becomes thinner in the immediate vicinity of the protein, a phenomenon that was also observed by Fowler et al.[16] Here we showed that the thinning occurred especially at the protein interface with the bilayer.

The dynamics of inhibitor egress from the active site were also modulated by the bilayer. The ΔPMF of the unbinding process is a valuable measure that was weakly correlated to the strength of the inhibitor. We observed that the ΔPMF changed drastically in the presence of solvent, indicating that the bilayer maintained a level of control over the dynamics of MAO B in and around the active site. The increase in the number of contacts between MAO B and an inhibitor in the presence of a bilayer further illustrated this point. Finally, the energies of interaction, when taken together, provided key information that will be useful in designing new inhibitors. The right combination of hydrophobic and hydrophilic groups within the same inhibitor is paramount to the success of binding, and our model of the active site with important residues highlighted is key in designing such an inhibitor. Static crystal structures alone cannot fully describe the intricacies of the protein−ligand relationship. Dynamic models such as this are invaluable in identifying important interactions that may otherwise be missed. It is important to note that the original K_i values (and, thus, the calculated ΔG_{dissoc} values) were determined in a buffer solution that contained reduced Triton X-100 detergent.[47] This may raise some concern as to how the simulation conditions (water or bilayer) can compare to experimental conditions (detergent solution). Hubalek et al. determined through a series of activity assays in detergent solution that the activity of MAO B was quite similar to that of MAO B in *in vivo* conditions.[48,49] Therefore, we remain confident that relative ΔG_{dissoc} values hold true and can be compared directly to our simulated values.

Recently, Colizzi et al. used a form of steered MD to pull several inhibitors from the active site of *Plasmodium falciparum* β-hydroxyacyl-ACP dehydratase, thereby using the resulting ΔPMF values to distinguish between active and inactive inhibitors.[50] Following that study, Jorgensen wrote a brief commentary in *Nature* describing the merits of steered MD simulations and its utility in drug discovery.[51] He questions whether the peak force applied during active site egress would correlate more strongly with inhibitor strength. In our study, we found that the peak force required to pull the inhibitor did not correlate more strongly with the strength of each inhibitor than did the ΔPMF value. However, the limitations of Jarzynski's equality have been well described.[52] The accuracy of ΔPMF measurements will continue to increase as the number of replicates increases and as the pulling speed and force constant in the spring decrease, each of which, in practice, increases the computing hours required to perform the simulation. That being said, despite the number of replicates we used

and the pulling conditions, we observed a very strong correlation between inhibitor strength and the sum of the per-residue energies of interactions from the energy profiles (Figures 9 and 10). We propose that this rubric be used in tandem with force and ΔPMF measurements to further discern between inhibitors of varying strength.

In summary, the implication of these observations is quite profound. Foremost, we have demonstrated that MAO B in a bilayer does not behave similarly to MAO B in solvent, especially pertaining to the active site and active site entrance dynamics. Therefore, when studying MAO B, particularly in the context of drug design, the correct model should always be to study this enzyme in a bilayer. This suggestion extends well beyond just MAO B and should be applied to any system studied by MD. Studying the biomolecules in the correct environment is key in obtaining accurate or meaningful results. Described herein are some important observations and implications that are useful to those taking a knowledge-based drug design approach to the design of powerful and reversible inhibitors of MAO B.

■ ASSOCIATED CONTENT

Supporting Information. Tables of inhibitor and cofactor parameters, tabulated ΔPMF and peak force values for the steered MD simulations, additional RMSF plots, and linear regression plots. This material is available free of charge via the Internet at http://pubs.acs.org.

■ AUTHOR INFORMATION

Corresponding Author

*E-mail: drbevan@vt.edu. Phone: 540-231-5040. Fax: 540-231-9070.

Funding Sources

This material is based upon work supported in part by the Macromolecular Interfaces with Life Sciences (MILES) Integrative Graduate Education and Research Traineeship (IGERT) of the National Science Foundation under Agreement No. DGE-0333378.

■ ACKNOWLEDGMENT

The authors thank Justin Lemkul for useful discussions regarding this project, James M. Tanko for allowing us the use of Titan, and the administrators of the Advanced Research Computing facility at Virginia Tech for computing hours.

■ ABBREVIATIONS

MAO B, monoamine oxidase B; FAD, flavin adenine dinucleotide; PDB, Protein Data Bank; MD, molecular dynamics; ATP, adenosine triphosphate; FMN, flavin mononucleotide; CHELP, charges derived from electrostatic potential; POPC, palmitoyloleoylphosphatidylcholine; POPE, palmitoyloleoylphosphatidylethanolamine; PME, particle mesh Ewald; P-LINCS, parallelized linear constraint solver; SPC, simple point charge; NVT, constant number of atoms, volume, temperature; NPT, constant number of atoms, pressure, temperature; APL, area per lipid; RMSD, root-mean-square deviation; RMSF, root-mean-square fluctuation; ΔPMF, potential of mean force; ΔG_{disso}, Gibbs free energy of dissociation.

■ REFERENCES

(1) Shih, J. C., Chen, K., and Ridd, M. J. (1999) Monoamine oxidase: From genes to behavior. *Annu. Rev. Neurosci. 22*, 197–217.

(2) Fowler, J. S., Volkow, N. D., Wang, G.-J., Logan, J., Pappas, N., Shea, C., and Macgregor, R. (1997) Age-related increases in brain monoamine oxidase B in living healthy human subjects. *Neurobiol. Aging 18*, 431–435.

(3) Tabakman, R., Lecht, S., and Lazarovici, P. (2004) Neuroprotection by monoamine oxidase B inhibitors: a therapeutic strategy for Parkinson's disease?. *BioEssays 26*, 80–90.

(4) Birkmayer, W., Knoll, J., Riederer, P., Youdim, M. B., Hars, V., and Marton, J. (1985) Increased life expectancy resulting from addition of L-deprenyl to Madopar treatment in Parkinson's disease: a longterm study. *J. Neural Transm. 64*, 113–127.

(5) Finberg, J. P. M., Lamensdorf, I., Commissiong, J. W., and Youdim, M. B. H. (1996) Pharmacology and neuroprotective properties of rasagiline. *J. Neural Transm. 48*, 95–101.

(6) Naoi, M., and Maruyama, W. (2009) Functional mechanism of neuroprotection by inhibitors of type B monoamine oxidase in Parkinson's disease. *Expert Rev. Neurother.*.

(7) Binda, C., Wang, J., Pisani, L., Caccia, C., Carotti, A., Salvati, P., Edmondson, D. E., and Mattevi, A. (2007) Structures of human monoamine oxidase B complexes with selective noncovalent inhibitors: Safinamide and coumarin analogs. *J. Med. Chem. 50*, 5848–5852.

(8) Binda, C., Newton-Vinson, P., Hubálek, F., Edmondson, D. E., and Mattevi, A. (2002) Structure of human monoamine oxidase B, a drug target for the treatment of neurological disorders. *Nat. Struct. Biol. 9*, 22–26.

(9) Edmondson, D. E., Binda, C., and Mattevi, A. (2004) The FAD binding sites of human monoamine oxidases A and B. *Neurotoxicology 25*, 63–72.

(10) Edmondson, D. E., Binda, C., and Mattevi, A. (2007) Structural insights into the mechanism of amine oxidation by monoamine oxidases A and B. *Arch. Biochem. Biophys. 464*, 269–276.

(11) Berman, H. M., Westbrook, J., Feng, Z., Gilliland, G., Bhat, T. N., Weissig, H., Shindyalov, I. N., and Bourne, P. E. (2000) The Protein Data Bank. *Nucleic Acids Res. 28*, 235–242.

(12) Tsugeno, Y., and Ito, A. (1997) A Key amino acid responsible for substrate selectivity of monoamine oxidase A and B. *J. Biol. Chem. 272*, 14033–14036.

(13) Hubálek, F., Binda, C., Khalil, A., Li, M., Mattevi, A., Castagnoli, N., and Edmondson, D. E. (2005) Demonstration of isoleucine 199 as a structural determinant for the selective inhibition of human monoamine oxidase B by specific reversible inhibitors. *J. Biol. Chem. 280*, 15761–15766.

(14) Geha, R. M., Rebrin, I., Chen, K., and Shih, J. C. (2001) Substrate and inhibitor specificities for human monoamine oxidase A and B are influenced by a single amino acid. *J. Biol. Chem. 276*, 9877–9882.

(15) Li, M., Binda, C., Mattevi, A., and Edmondson, D. E. (2006) Functional role of the "aromatic cage" in human monoamine oxidase B: Structures and catalytic properties of Tyr435 mutant proteins. *Biochemistry 45*, 4775–4784.

(16) Fowler, P. W., Balali-Mood, K., Deol, S., Coveney, P. V., and Sansom, M. S. P. (2007) Monotopic enzymes and lipid bilayers: A Comparative Study. *Biochemistry 46*, 3108–3115.

(17) Apostolov, R., Yonezawa, Y., Standley, D. M., Kikugawa, G., Takano, Y., and Nakamura, H. (2009) Membrane attachment facilitates ligand access to the active site in monoamine oxidase A. *Biochemistry 48*, 5864–5873.

(18) Binda, C., Li, M., Hubálek, F., Restelli, N., Edmondson, D. E., and Mattevi, A. (2003) Insights into the mode of inhibition of human mitochondrial monoamine oxidase B from high-resolution crystal structures. *Proc. Natl. Acad. Sci. U. S. A. 100*, 9750–9755.

(19) Binda, C., Hubálek, F., Li, M., Herzig, Y., Sterling, J., Edmondson, D. E., and Mattevi, A. (2005) Binding of rasagiline-related inhibitors to human monoamine oxidases: A kinetic and crystallographic analysis. *J. Med. Chem. 48*, 8148–8154.

(20) Case, D. A., Darden, T. A., Cheatham III, T. E., Simmerling, C. L., Wang, J., Duke, R. E., Luo, R., Crowley, M., Walker, R. C., Zhang, W., Merz, K. M., Wang, B., Hayik, S., Roitberg, A., Seabra, G., Kolossvery, I., Wong, K. F., Paesani, F., Vanicek, J., Wu, X., Brozell, S. R., Steinbrecher, T., Gohlke, H., Yang, L., Tan, C., Mongan, J., Hornak, V., Cui, G., Mathews, D. H., Seetin, M. G., Sagui, C., Babin, V., and Kollman, P. A. (2008) AMBER 10, University of California, San Francisco, CA.

(21) Schüttelkopf, A. W., and van Aalten, D. M. F. (2004) PRODRG: a tool for high-throughput crystallography of protein-ligand complexes. *Acta Crystallogr. D60*, 1355–1363.

(22) Lemkul, J. A., Allen, W. J., and Bevan, D. R. (2010) Practical considerations for building GROMOS-compatible small molecule topologies. *J. Chem. Inf. Model. 50*, 2221–2235.

(23) Chirlian, L. E., and Francl, M. M. (1987) Atomic charges derived from electrostatic potentials: A detailed study. *J. Comput. Chem. 8*, 894–905.

(24) Berger, O., Edholm, O., and Jähnig, F. (1997) Molecular dynamics simulations of a fluid bilayer of dipalmitoylphosphatidylcholine at full hydration, constant pressure, and constant temperature. *Biophys. J. 72*, 2002–2013.

(25) Tieleman, D. P., Sansom, M. S. P., and Berendsen, H. J. C. (1999) Alamethicin helices in a bilayer and in solution: Molecular dynamics simulations. *Biophys. J. 76*, 40–49.

(26) van Meer, G., Voelker, D. R., and Feigenson, G. W. (2008) Membrane lipids: Where they are and how they behave. *Nat. Rev. Mol. Cell Biol. 9*, 112–124.

(27) Hess, B., Kutzner, C., van der Spoel, D., and Lindahl, E. (2008) GROMACS 4: Algorithms for highly efficient, load-balanced, and scalable molecular simulation. *J. Chem. Theory Comput. 4*, 435–447.

(28) Darden, T., York, D., and Pedersen, L. G. (1993) Particle mesh Ewald: An N-log(N) method for Ewald sums in large systems. *J. Chem. Phys. 98*, 10089–10092.

(29) Essmann, U., Perera, L., Berkowitz, M. L., Darden, T., Lee, H., and Pedersen, L. G. (1995) A smooth particle mesh Ewald method. *J. Chem. Phys. 103*, 8577–8593.

(30) Hess, B., Bekker, H., Berendsen, H. J. C., and Fraaije, J. G. E. M. (1997) LINCS: A linear constraint solver for molecular simulations. *J. Comput. Chem. 18*, 1463–1472.

(31) Hess, B. (2007) P-LINCS: A parallel linear constraint solver for molecular simulation. *J. Chem. Theory Comput. 4*, 116–122.

(32) Berendsen, H. J. C., Postma, J. P. M., van Gunsteren, W. F., and Hermans, J. (1981) *Intermolecular Forces, Interaction Models for Water in Relation to Protein Hydration*, D. Reidel Publishing Co., Dordrecht, The Netherlands.

(33) Berendsen, H. J. C., Postma, J. P. M., van Gunsteren, W. F., DiNola, A., and Haak, J. R. (1984) Molecular dynamics with coupling to an external bath. *J. Chem. Phys. 81*, 3684–3690.

(34) Nosé, S. (1984) A molecular dynamics method for simulations in the canonical ensemble. *Mol. Phys. 52*, 255–268.

(35) Hoover, W. G. (1985) Canonical dynamics: Equilibrium phase-space distributions. *Phys. Rev. A 31*, 1695–1697.

(36) Parrinello, M., and Rahman, A. (1981) Polymorphic transitions in single crystals: A new molecular dynamics method. *J. Appl. Phys. 52*, 7182–7190.

(37) Nosé, S., and Klein, M. L. (1983) Constant pressure molecular dynamics for molecular systems. *Mol. Phys. 50*, 1055–1076.

(38) Kandt, C., Ash, W. L., and Tieleman, D. P. (2007) Setting up and running molecular dynamics simulations of membrane protiens. *Methods 41*, 475–488.

(39) DeLano, W. L. (2002) *The PyMOL User's Manual*, DeLano Scientific, Palo Alto, CA.

(40) Turner, P. J. (2002) *Grace*, Center for Coastal and Land-Margin Research Oregon Graduate Institute of Science and Technology, Beaverton, OR.

(41) Allen, W. J., Lemkul, J. A., and Bevan, D. R. (2009) GridMAT-MD: A grid based membrane analysis tool for use with molecular dynamics. *J. Comput. Chem. 30*, 1952–1958.

(42) Kučerka, N., Tristram-Nagle, S., and Nagle, J. F. (2005) Structure of fully hydrated fluid phase lipid bilayers with monounsaturated chains. *J. Membr. Biol. 208*, 193–202.

(43) Rand, R. P., Fuller, N., Parsegian, V. A., and Rau, D. C. (1998) Variation in hydration forces between neutral phospholipid bilayers: Evidence for hydration attraction. *Biochemistry 27*, 7711–7722.

(44) Hall, S. E., Roberts, K., and Vaidehi, N. (2009) Position of helical kinks in membrane protein crystal structures and the accuracy of computational prediction. *J. Mol. Graph. Model. 27*, 944–950.

(45) Edmondson, D. E., Binda, C., Wang, J., Upadhyay, A. K., and Mattevi, A. (2009) Molecular and mechanistic properties of the membrane-bound mitochondrial monoamine oxidases. *Biochemistry 48*, 4220–4230.

(46) Jarzynski, C. (1997) Nonequilibrium equality for free energy differences. *Phys. Rev. Lett. 78*, 2690–2693.

(47) Hubálek, F., Binda, C., Li, M., Herzig, Y., Sterling, J., Youdim, M. B. H., Mattevi, A., and Edmondson, D. E. (2004) Inactivation of purified human recombinant monoamine oxidases A and B by rasagiline and its analogues. *J. Med. Chem. 47*, 1760–1766.

(48) Sterling, J., Veinberg, A., Lerner, D., Goldenberg, W., Levy, R., Youdim, M., and Finberg, J. (1998) R)(+)-N-propargyl-1-aminoindan (rasagiline) and derviatives: highly selective and potent inhibitors of monoamine oxidase B. *J. Neural. Transm. 52*, 301–305.

(49) Sterling, J., Herzig, Y., Goren, T., Finkelstein, N., Lerner, D., Goldenberg, W., Miskolczi, I., Molnar, S., Rantal, F., Tamas, T., Toth, G., Zagyva, A., Zekany, A., Lavian, G., Gross, A., Friedman, R., Razin, M., Huang, W., Krais, B., Chorev, M., Youdim, M. B., and Weinstock, M. (2002) Novel dual inhibitors of AChE and MAO derived from hydroxy aminoindan and phenethylamine as potential treatment for Alzheimer's disease. *J. Med. Chem. 45*, 5260–5279.

(50) Colizzi, F., Perozzo, R., Scapozza, L., Recanatini, M., and Cavalli, A. (2010) Single-molecule pulling simulations can discern active from inactive enzyme inhibitors. *J. Am. Chem. Soc. 132*, 7361–7371.

(51) Jorgensen, W. L. (2010) Drug discovery: Pulled from a protein's embrace. *Nature 466*, 42–43.

(52) Baştuğ, T., Chen, P.-C., Patra, S. M., and Kuyucak, S. (2008) Potential of mean force calculations of ligand binding to ion channels from Jarzynski's equality and umbrella sampling. *J. Chem. Phys. 128*, 155104.155101–155104.155109.